III

Publication III

V. Hynönen, T. Kurki-Suonio, W. Suttrop, R. Dux, K. Sugiyama, and the ASDEX Upgrade Team (2007). Surface loads and edge fast ion distribution for co- and counter-injection in ASDEX Upgrade. *Plasma Physics and Controlled Fusion*[†] **49**(2) 151–174.

Surface loads and edge fast ion distribution for co- and counter-injection in ASDEX Upgrade

V Hynönen[1]**, T Kurki-Suonio**[1]**, W Suttrop**[2]**, R Dux**[2]**, K Sugiyama**[3] **and the ASDEX Upgrade Team**[2]

[1] Helsinki University of Technology, Association Euratom-TEKES, FI-02015 TKK, Finland
[2] Max-Planck-Institut für Plasmaphysik, Euratom Association, D-85740 Garching, Germany
[3] Interdisciplinary Graduate School of Engineering Sciences, Kyushu University, Hakozaki 6-10-1, Higashi-ku, Fukuoka 812-8581, Japan

E-mail: ville.hynonen@tkk.fi

Abstract

The fast particle flux onto the material surfaces and the fast ion edge distribution are compared between ASDEX Upgrade H-mode and quiescent H-mode (QH-mode) in the presence of toroidal ripple and radial electric field E_r by using the orbit-following Monte Carlo code ASCOT. So far, the QH-mode has been obtained only with counter-injection of the neutral beams. The wall load caused by co-injected beams in H-mode is small and without ripple it is negligible. With counter-injection (QH-mode case), the wall load is substantial even without the ripple. The ripple always increases the wall load, but the divertor load is either decreased or is unchanged. The effect of E_r alone is small, but it boosts the ripple-trapping of beam particles near the location of its maximum absolute value on the horizontal midplane. The fast ion density and its gradient in the pedestal region are higher for counter-injected than for co-injected particles. The ripple decreases the density gradient in both the cases. To make a connection with the experiment, the flux of high-energy tritons from beam–plasma interactions onto the surfaces is evaluated. The simulated flux of tritons impinging on the material surfaces is in qualitative agreement with the measured tritium distribution on the wall and divertor.

(Some figures in this article are in colour only in the electronic version)

1. Introduction

The standard H-mode operation is characterized by ELMs, violent bursts of energy and particles, which can lead to unacceptable loads onto plasma-facing components [1]. On

the other hand, ELMs play a crucial role in controlling density and exhausting impurities. Therefore finding the means to moderate or eliminate ELMs, while keeping stationary density and impurity content, is of paramount importance, especially for fusion reactors such as ITER. The improved confinement regimes hot ion mode [2] and VH-mode [3] are characterized by non-stationary ELM-free periods terminated by an MHD event. However, in the so-called quiescent H-mode (QH-mode) ELMs are replaced by more continuous, benign MHD behaviour called the edge harmonic oscillations (EHO) [4] enabling stationary plasma density and radiation level. The QH-mode was originally discovered in DIII-D in 1999 [5] and has thereafter been reproduced in ASDEX Upgrade [6] and JET [4]. A similar H-mode behaviour has also been reported at JT-60U [7]. So far, the QH-mode has been obtained only with counter-injection of the neutral beams.

The EHO-operation of plasma edge would be ideal in a fusion reactor: it facilitates density control and impurity exhaust while leaving the good core confinement intact. It is not clear what is the trigger for EHO nor is it understood what suppresses the ELMs, but since counter neutral beam injection (NBI) is a prerequisite, fast ions probably play a role by affecting the edge stability properties and thus, ELMs.

Playing a role in the QH-mode is an important aspect of fast ions, but they also deserve careful attention in a more general sense. In high performance plasmas, fast ions are expected to contribute significantly to the particle and power loads on material surfaces. Particularly in ITER and other future reactors, the fusion alpha particles have to be confined during their slowing down process to avoid large heat and particle loads on the first wall and the divertor. Furthermore, while slowing down, the alpha particles need to heat the bulk plasma without driving instabilities. In the present-day experiments fusion reactions are largely absent, with the exception of the tritium campaigns at TFTR [8] and JET [9]. Nevertheless the fast ions created by NBI and radio frequency heating (ICRH) can, under some conditions, e.g. with enhanced ripple, cause significant damage on the material surfaces.

All issues related to fast ions become even more interesting when the non-axisymmetry of the tokamak magnetic field is taken into account. Toroidal ripple is bound to affect not only the losses but also the fast ion population at the edge. The former might play a significant role in the L–H transition, while the latter can affect the edge stability. The effect of the toroidal ripple on fast particle losses has been evaluated using the orbit-following Monte Carlo code ASCOT [10]. A realistic three-dimensional ripple obtained from vacuum field calculations was used in these simulations. Earlier, the effect of ripple on radial electric field formation [11] was analysed using a simpler, two-dimensional model for the ripple.

In this paper we investigate all the aforementioned issues related to the edge fast ion population in tokamak geometry. In the QH-mode, the drift orbits of counter-injected neutral beam ions open outwards causing prompt losses to the walls, but at the same time feeding high energy particles into the edge region. Indeed, ASCOT simulations have already shown that with counter-injection, a significant fast ion population exists in the edge pedestal region [4]. Here we have studied the subject further by simulating co- and counter-injected neutral beam ions taking into account the effects of finite toroidal ripple and the radial electric field E_r typical of a QH-mode discharge. The next section describes the ASCOT code and, in particular, the new ripple model. Subsequently the effects of E_r and ripple on fast ion edge distribution and fast ion losses together with wall loads are discussed. Finally, the surface distribution of tritons from beam–plasma and thermal D–D reactions is studied.

2. The ASCOT code

2.1. Simulation model

The ASCOT code is a guiding-centre orbit-following code for studies of charged particle behaviour in tokamaks and stellarators [12]. ASCOT accurately accounts for all neoclassical physics, and since the anomalous transport is partially suppressed in the edge region, this makes ASCOT well suited for H-mode edge studies. Especially for fast particles the anomalous transport does not play a significant role. The test particles are followed along their guiding-centre orbits determined by the $E \times B$, gradient and curvature drifts, collisions as well as polarization and gyroviscosity drifts. The particle following takes place in a five-dimensional phase space with three configuration and two velocity space coordinates. In the configuration space either the Cartesian or Boozer coordinate system can be used inside the separatrix. The Cartesian coordinates are always used outside the separatrix. The fifth order Runge–Kutta with error checking is used for orbit integration whenever Cartesian coordinates are used. The Boozer coordinate system is intrinsically more accurate than the Cartesian, and therefore the optional 4th order Runge–Kutta can be used for integration inside the plasma. The effects of particle collisions are modelled with Monte Carlo operators derived from the Fokker–Planck equation.

The particles are followed in a true-to-life geometry. The magnetic and plasma background data are obtained from experimental databases. The toroidal field (TF) component is the sum of the vacuum field and the TF due to the diamagnetic effects. The primary data used in calculating the poloidal magnetic field is the poloidal flux matrix obtained from equilibrium calculations. The resulting ASCOT background file contains the interpolated poloidal flux ψ_p, the normalized minor radius $\rho = \rho_p = \sqrt{\psi_p}$ and the magnetic field components as 600×600 arrays in R and z.

In figure 1 an example of the ASDEX Upgrade vessel geometry and magnetic background is shown. As a default the toroidal dependence of the magnetic field is neglected, but recently a new three-dimensional model for toroidal ripple has been programmed into ASCOT. The new model was originally developed to simulate the JET ripple experiments planned for the future. In JET it is possible to vary the ripple strength during the discharge by altering the current in even and odd-numbered field coils. When the model is used, the total magnetic field is of the form

$$B_R(R, z, \phi) = B_{R,0} + A_1 B_{R,1} \sin(N_1\phi) + A_2 B_{R,2} \sin(N_2\phi), \tag{1}$$

$$B_z(R, z, \phi) = B_{z,0} + A_1 B_{z,1} \sin(N_1\phi) + A_2 B_{z,2} \sin(N_2\phi), \tag{2}$$

$$B_\phi(R, z, \phi) = B_{\phi,0} + A_1 B_{\phi,1} \cos(N_1\phi) + A_2 B_{\phi,2} \cos(N_2\phi). \tag{3}$$

Here the different order components are functions of R and z, $B_{\cdot,i} = B_{\cdot,i}(R, z)$, where the dot stands for the component (R, z, ϕ) and $i = 0, 1, 2$ and $N_2 = 2N_1$ is the number of toroidal field coils. The 0th order terms $B_{\cdot,0}(R, z)$ form the axisymmetric magnetic background. Through the constants $A_{1,2}$, which depend on the coil currents I_{even} and I_{odd}, it is possible to change the ripple strength in the simulation without touching the large arrays representing the (R, z)-dependence of the perturbative terms $B_{\cdot,i}(R, z)$, $i = 1, 2$ obtained from the vacuum field calculations.

This representation of the magnetic field with ripple has been derived by writing separately the Fourier expansions of the magnetic field generated by the even and odd-numbered field coils and adding them together. The third and higher order terms have been neglected. Despite the JET ripple experiments being the primary application, the model is general enough to be used for any tokamak. In normal operation of JET, as well as in any other tokamak, the currents
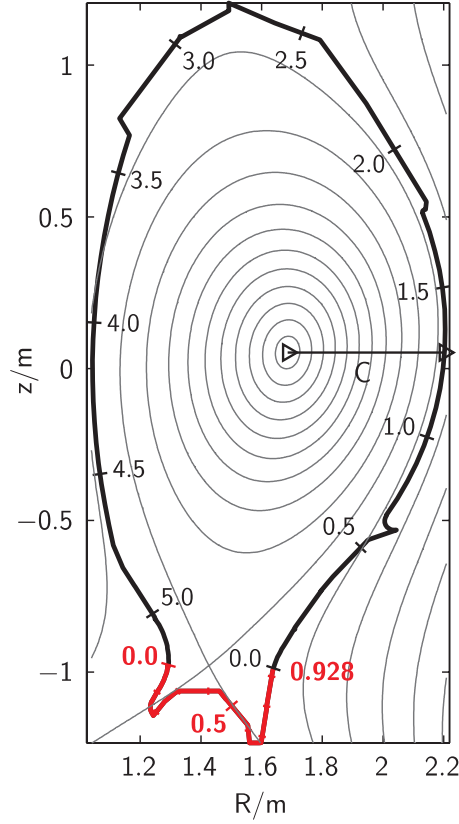
Figure 1. ASDEX Upgrade wall geometry used in the ASCOT simulations together with the poloidal flux surfaces for ASDEX Upgrade pulse #17695 at $t = 5.6$ s. Divertor and wall coordinates, s_d and s_w, used for the particle and power flux profiles, are shown outside (red/bold-faced font) and inside (black/grotesque font) the wall, respectively. In this coordinate system the outer and inner divertor baffles, roughly at $s_w = 0.0$–0.4 m and at $s_w = 4.8$–5.1 m, respectively, are considered part of the wall. The line C in the outer midplane is used in the calculation of the radial electric field.

in even and odd numbered coils are the same, $I_{\text{even}} = I_{\text{odd}}$. In this case we have $A_1 = 0$, and the total magnetic field simplifies to

$$B_R(R, z, \phi) = B_{R,0} + A_2 B_{R,2} \sin(N_2 \phi), \tag{4}$$

$$B_z(R, z, \phi) = B_{z,0} + A_2 B_{z,2} \sin(N_2 \phi), \tag{5}$$

$$B_\phi(R, z, \phi) = B_{\phi,0} + A_2 B_{\phi,2} \cos(N_2 \phi). \tag{6}$$

The radial electric field E_r is not a flux function but the static potential V is. For this reason, in ASCOT the radial electric field is expressed as the derivative of the potential with respect to the normalized minor radius,

$$\tilde{E}(\rho) = \frac{\mathrm{d}V}{\mathrm{d}\rho}. \tag{7}$$

Expressed in this way, the radial electric field can be imported into ASCOT as a radial profile. Alternatively, if no experimental data are available, it can either be represented by simple analytic models, such as piecewise constant or third order polynomial, or its neoclassical, ambipolar value can be calculated from the plasma profiles [13]. During the simulation, $\tilde{E}(\rho)$

is interpolated according to the selected form of representation and converted back to physical units by scaling by the local value of $|\nabla\rho|^{-1}$.

The experimental data, if available, have to be converted to $dV/d\rho$ units. The simplest way of doing this is to integrate the given E_r and subsequently differentiate the obtained potential with respect to ρ.

2.2. Distributions and wall load

In the ASCOT simulations of NBI-born fast ions, the test particles represent a particle source. The weight of a single test particle is roughly the number of real particles entering the plasma per second divided by the number of test particles. Each test particle is followed until one of the following end criteria is reached:

(1) the specified particle tracing time is exceeded,
(2) the maximum CPU time per test particle is exceeded,
(3) the specified lower limit of particle velocity is reached (thermalization) and
(4) the particle hits the wall or the divertor.

The physically meaningful end criteria in NBI simulations are numbers (3) and (4). Since we are only interested in fast particles, the usual thermalization criterium is reaching twice the local thermal velocity. The maximum particle tracing time has to be large enough so that all the test particles have enough time to thermalize. In a successful simulation there should be no test particles exceeding the CPU limit, since this usually indicates some sort of numerical problem.

While the particles are followed, information about each integration time step is accumulated into various distributions, the most important ones being the different phase space densities. The four-dimensional space spanned by the normalized minor radius ρ, the poloidal angle θ and the parallel and the perpendicular velocities $v_\parallel$ and $v_\perp$ is divided into uniformly spaced cells. The total time spent in the cells is recorded, multiplied by the ratio of the particle source rate to the number of test particles and divided by the phase space volume of the cell giving the four-dimensional steady-state phase space density in units of $\mathrm{m}^{-3}\,(\mathrm{m/s})^{-3}$.

Because four-dimensional quantities as such are impossible to visualize, different integrals of the four-dimensional distribution are studied instead. Usually the integration is performed over the whole range of values for one or more coordinates, but it can also be of interest to consider a slice of the four-dimensional distribution by integrating over some specific range of, for example, the poloidal angle. The most frequently used distributions obtained this way are (units in square brackets) the following.

Radial density. Density of particles as function of ρ [m^{-3}].
Total velocity distribution. Phase space density of particles as function of ρ and total velocity v_{tot} [$\mathrm{m}^{-3}\,(\mathrm{m/s})^{-3}$].
Parallel velocity distribution. Phase space density of particles as function of ρ and $v_\parallel$ [$\mathrm{m}^{-3}\,(\mathrm{m/s})^{-1}$].
Perpendicular velocity distribution. Phase space density of particles as function of ρ and $v_\perp$ [$\mathrm{m}^{-3}\,(\mathrm{m/s})^{-2}$].

Whenever a test particle hits a material surface, its final location ($R_{\mathrm{end}}, z_{\mathrm{end}}, \phi_{\mathrm{end}}$), its weight and its energy multiplied by the weight are recorded. Using this information it is possible to calculate the particle and power flux onto the divertor and the wall. The wall contour shown in figure 1 is divided into 47 segments in the divertor region (red part of the contour) and 104 segments in the wall region, giving the poloidal resolution of about 2 cm and 5 cm, respectively. The amount of particles and energy hitting each segment is calculated
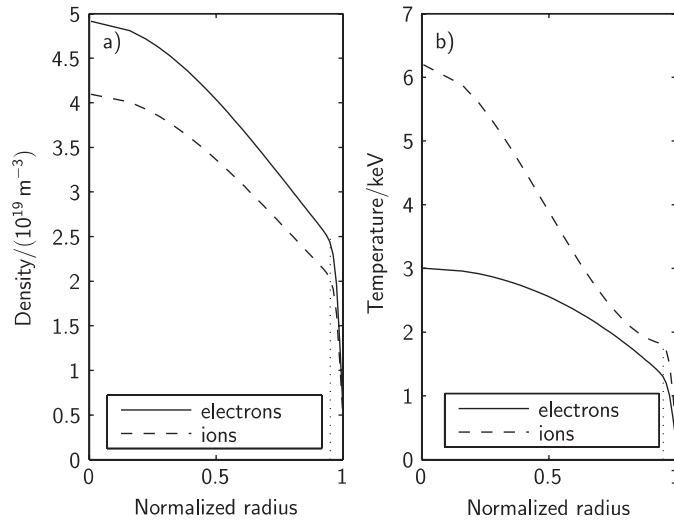
Figure 2. (*a*) Density and (*b*) temperature profiles of electrons (——) and ions (- - - -) for the ASDEX Upgrade QH-mode discharge #17695 at $t = 5.6$ s. The effective charge number $Z_{eff} = 2$ and 4% of carbon is assumed in the plasma. The pedestal ($\cdots\cdots$) is roughly at $\rho = 0.95$.

from the recorded wall data and divided by the area of the segment. The resulting particle and power flux are in units of $m^{-2}\,s^{-1}$ and $W\,m^{-2}$, respectively.

3. NBI-born fast ions

In this section we set out to study some of the critical issues related to fast ions by comparing the ASDEX Upgrade QH-mode and H-mode. The fast ion distribution in the edge and the particle and power fluxes onto the material surfaces are simulated using ASCOT. The plasma background and the magnetic equilibrium for the QH-mode simulations were extracted from the ASDEX Upgrade database for the counter-injection discharge #17695 at $t = 5.6$ s (see figure 1). The temperature and density profiles for the discharge are shown in figure 2. A vacuum background is assumed for the scrape-off layer (SOL). The initial locations of 1057 test particles, corresponding to two counter-injected neutral beams (beam lines 2 and 3, both with a nominal injection energy $E = 60$ keV and a radius of tangency $R_T = 0.93$ m), were calculated using the FAFNER code [14]. Full, half and one-third energy components were included in the FAFNER output. The nominal heating power produced by the two beams in the discharge was 5.141 MW, but due to shine-through the actual particle fluence is $\Gamma_{NBI} = 7.3 \times 10^{20}\,s^{-1}$, corresponding to a heating power of 4.8 MW. In order to get better statistics, the test particles created by FAFNER were replicated by a factor of 50 to form an ensemble of 52 850 test particles for ASCOT simulations.

To minimize the number of factors affecting the comparison, the same background and test particle data were used to simulate an H-mode with co-injected neutral beams. In a QH-mode discharge the plasma current is negative and the toroidal component of the magnetic field positive, so that the ∇B-drift points upwards. Thus the banana orbits of the counter-injected NBI ions having a positive initial pitch $(= v_\parallel/v)$ open outwards. Such an orbit is called ill-confined as opposed to a well-confined orbit of a co-injected ion having a negative initial pitch. A virtual H-mode discharge was created from the original QH-mode data by reversing
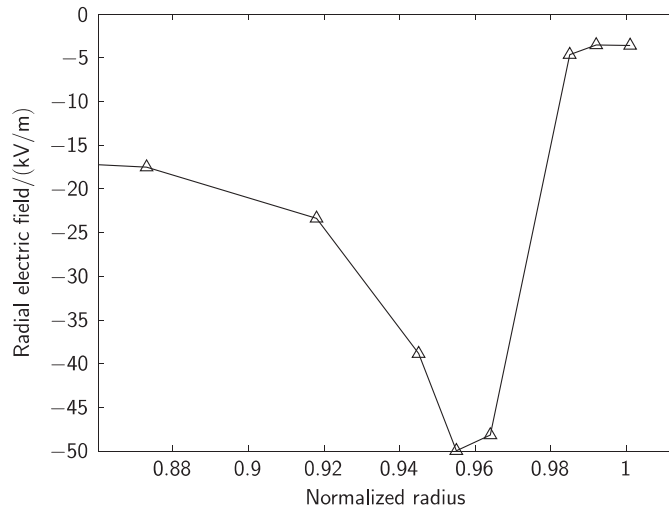
Figure 3. The radial electric field E_r profile used in the co- and counter-injection simulations in kV m^{-1} (——). The profile is calculated from the edge QH-mode perpendicular velocity $u_\perp$ profile for the counter-NBI discharge #16111 [15].

the signs of the plasma current and toroidal magnetic field in the magnetic background data and the sign of the pitch in the test particle data. For both counter- and co-injection the following four simulations with different combinations of the toroidal ripple and radial electric field E_r were carried out:

(1) no magnetic ripple, no radial electric field,
(2) no magnetic ripple, typical QH-mode radial electric field,
(3) finite toroidal ripple, no radial electric field and
(4) both finite ripple and typical QH-mode radial electric field.

The QH-mode perpendicular velocity $u_\perp$ profile measured from the counter-NBI discharge #16111 using Doppler reflectometry [15] was used in the calculation of the E_r profile. It was assumed that the perpendicular velocity arises solely from the $\boldsymbol{E}_r \times \boldsymbol{B}_\phi$-drift and that the $u_\perp$ profile was measured along the midplane in the low field side. The expression for E_r is then simply $E_r = u_\perp B$. The resulting E_r profile is illustrated in figure 3. The same E_r profile was used both in the QH-mode and H-mode simulations, again to keep the comparison as simple as possible. This overestimates the effects of E_r in the H-mode, because the $u_\perp$ measured from the ELMy H-mode phase of the same discharge is lower than the QH-phase $u_\perp$. For more accurate results it would be necessary to use the H-mode phase E_r profile and magnetic background for the co-injection simulations.

A radial electric field is likely to exist also in the SOL where its value is assumed positive. Since measurements of such a field are not readily available, we have omitted it in the simulations. However, as found in [4], a positive radial electric field narrows the orbits of the co-injected ions and widens them for counter-injected ones. This could have an effect on the shape of the deposition profiles on the vessel wall.

3.1. Wall and divertor load

The simulated wall and divertor loads presented below can be compared with the steady-state loads in the experiment. The stationary power load on the ASDEX Upgrade divertor target
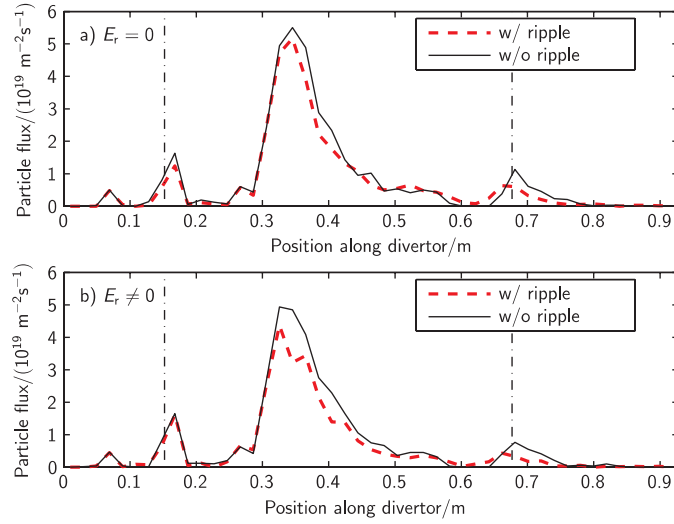
Figure 4. The particle flux onto the divertor in the axisymmetric case (——) and in the case with finite toroidal ripple (red/grey thick - - - -) for co-injected neutral beams (H-mode). (*a*) No E_r. (*b*) Typical QH-mode E_r shown in figure 3. The strike-points are marked with vertical dash–dot lines, and the coordinates are illustrated in figure 1.

plates in H-mode is between 1 and 2 MW m^{-2}, depending on the NBI input power [16]. On the wall the leading edge of the limiters receives a power flux of up to 1 MW m^{-2} in between ELMs [17]. During an ELM the loads increase by about a factor of 10 both on the divertor and on the wall.

We first simulate the virtual H-mode, i.e. the co-injection discharge created by reversing the signs in the background data. On the divertor both the ripple and E_r have little effect on the shape and magnitude of the particle flux as can be seen in figure 4. The shape itself is interesting, because the majority of the particles end up in the private flux region ($s_d = 0.25$– 0.6 m). Figure 5 shows a particle orbit terminating at the dome top. The banana tips of the orbit are moving further into the high field side widening the orbit before the particle escapes from the plasma. This suggests that the particles whose pitch is increased by the collisions are likely to end up in the private flux region.

The immediate observation about the wall load, shown in figure 6, is that there are only a few particles hitting the wall structures in the axisymmetric case regardless of the radial electric field. With the ripple the wall load can be compared with the peak particle flux at the divertor, which is roughly 5.5×10^{19} m^{-2} s^{-1}. Without the radial electric field there is moderate particle flux, of about 10% of the maximum particle flux at the divertor, at the lower part of the wall ($s_w = 0.0$–1.0 m) and below the guard limiter ($s_w \approx 1.7$ m) on the low field side. With the E_r the wall load is slightly diminished in the interval $s_w = 0.0$–0.6 m, but a new peak appears at $s_w \approx 0.9$ m with a magnitude of about 20% of the peak divertor load. The R-coordinate of the peak is $R \approx 2.1$ m, which on the horizontal midplane corresponds to $\rho \approx 0.96$. This matches perfectly with the minimum of the E_r profile (see figure 3). The peak in the wall load is therefore likely to be caused by particles which have been trapped due to the combined effect of the E_r and the ripple. The trapped particles drift downwards in the direction of the ∇B-drift and end up roughly at the same spot on the wall.

Tables 1 and 2 show the breakdown of the particle fluence and the incident power, respectively, between the wall and the divertor. By dividing the incident power by the particle
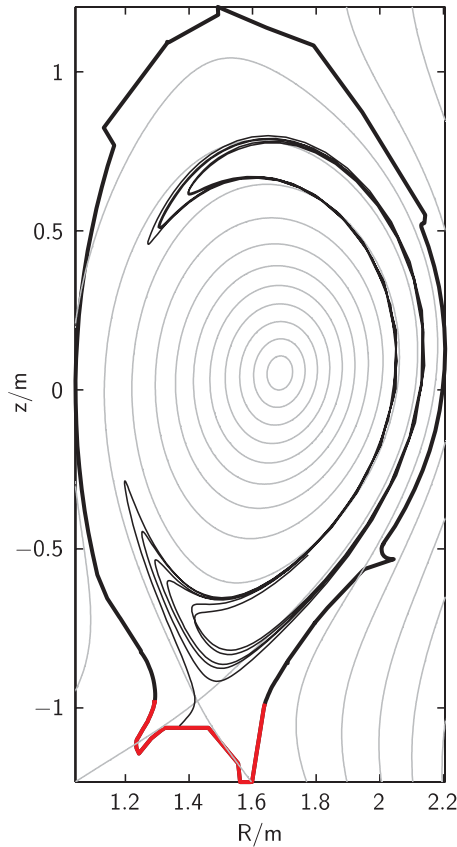
Figure 5. A particle orbit terminating on the dome top in the private flux region.

fluence we obtain the average energy of particles hitting the material surfaces, shown in table 3. In all the co-injection simulations the average energy of the particles hitting the divertor is roughly the same, a little below 20 keV. However, the average energy depends on the position along the divertor. The energy of the particles is higher at the strike-point ($s_d \approx 0.15$ m) and at $s_d \approx 0.27$ m where the $\rho = 1$ surface is closest to the high field side of the septum (see figure 1). This can be seen by comparing the particle flux to the power flux shown in figure 7, in which the side peaks at $s_d \approx 0.15$ m and $s_d \approx 0.27$ m are higher compared with the main peak in figure 4. These high-energy particles also show up in the energy distribution shown in figure 8.

Without the ripple the number of test particles hitting the wall is too small to make a reliable estimate of the average energy. With the ripple the average energies are higher on the wall than on the divertor, especially with E_r. The energy distribution on the wall is shown in more detail in figure 9. The power flux on the wall (not shown) is almost identical in shape to the particle flux, the peaks being roughly $30\,\mathrm{kW\,m^{-2}}$ and $50\,\mathrm{kW\,m^{-2}}$ with and without E_r, respectively. Since the ripple introduces toroidal dependence to the particle flux onto the wall, as illustrated in figure 10 for the co-injection simulations with ripple, the actual peak power fluxes could be even higher. The toroidal distribution of particle losses in co- and counter-injection simulations will be discussed in more detail at the end of this section.
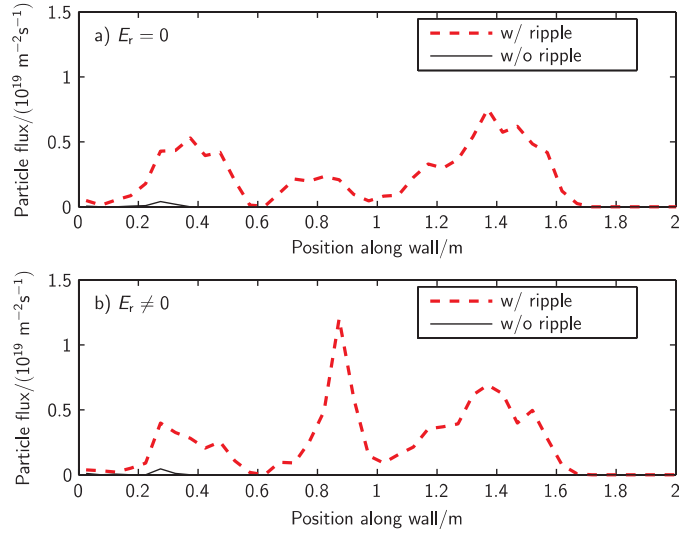
Figure 6. The particle flux onto the wall structures in the axisymmetric case (——) and in the case with finite toroidal ripple (red/grey thick - - - -) for co-injected neutral beams (H-mode). (*a*) No E_r. (*b*) Typical QH-mode E_r, shown in figure 3. The particle flux is zero in the region $s_w > 2$m in all the shown cases. The coordinates are illustrated in figure 1.

Table 1. The breakdown of the particle fluence between the wall and the divertor. Percentages of the NBI source rate $\Gamma_{NBI} = 7.3 \times 10^{20} \, s^{-1}$ shown in parentheses.

	Fluence ($10^{19} \, s^{-1}$) (co-injection)		Fluence ($10^{19} \, s^{-1}$) (counter-injection)	
Simulation	Wall	Divertor	Wall	Divertor
No ripple, no E_r	0.05 (0.07%)	6.4 (8.7%)	6.9 (9.5%)	13 (18%)
Only E_r	0.04 (0.06%)	6.0 (8.2%)	7.2 (9.9%)	12 (17%)
Only ripple	5.7 (7.8%)	5.7 (7.7%)	15 (20%)	9.8 (13%)
Both ripple and E_r	6.2 (8.5%)	4.8 (6.6%)	16 (22%)	7.6 (10%)

Table 2. The breakdown of the incident power between the wall and the divertor. Percentages of the total NBI power 4.8 MW shown in parentheses.

	Power (kW) (co-injection)		Power (kW) (counter-injection)	
Simulation	Wall	Divertor	Wall	Divertor
No ripple, no E_r	1.9 (0.04%)	180 (3.7%)	480 (10%)	420 (8.8%)
Only E_r	1.5 (0.03%)	170 (3.6%)	490 (10%)	370 (7.7%)
Only ripple	230 (4.7%)	170 (3.6%)	840 (17%)	330 (6.9%)
Both ripple & E_r	270 (5.7%)	150 (3.1%)	910 (19%)	250 (5.2%)

Next we simulate the case with the counter-injected neutral beams corresponding to the QH-mode. The striking difference between co- and counter-injection simulations is that in the latter, as shown in figure 11, there is significant particle flux onto the wall even in the axisymmetric case. This is to be expected since the counter-injected particles are born on ill-confined orbits, as discussed at the beginning of this section, and thus there are prompt

Table 3. The average energy E_{ave} of particles hitting the divertor and the wall in co- and counter-injection simulations.

Simulation	E_{ave} (keV) (co-injection)		E_{ave} (keV) (counter-injection)	
	Wall	Divertor	Wall	Divertor
No ripple, no E_{r}	25[a]	17	43	20
Only E_{r}	21[a]	18	42	19
Only ripple	25	19	35	21
Both ripple and E_{r}	28	19	36	21

[a] Unreliable due to low statistics.
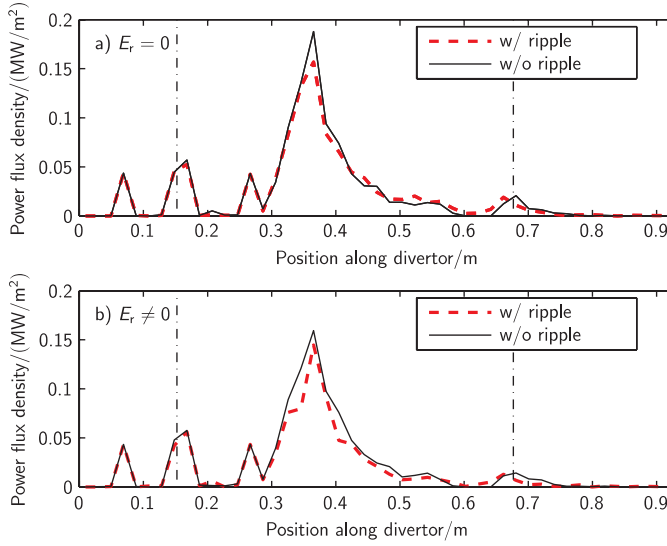
Figure 7. The power flux onto the divertor in the axisymmetric case (——) and in the case with finite toroidal ripple (red/grey thick – – –) for co-injected neutral beams (H-mode). (*a*) No E_{r}. (*b*) Typical QH-mode E_{r} shown in figure 3. The strike-points are marked with vertical dash–dot lines, and the coordinates are illustrated in figure 1.

losses to the walls. There are two large peaks in the wall particle flux at $s_{\text{w}} \approx 0.4$ m and at $s_{\text{w}} \approx 1.7$ m, the latter being the region near or at the guard limiter. These are the points that are closest to the plasma. There are some smaller peaks in the passive stabilizer loop ($s_{\text{w}} = 1.8$–2.5 m) and in the upper divertor ($s_{\text{w}} = 2.5$–3.2 m). With the ripple a larger peak forms in the passive stabilizer loop area, and with E_{r} added on top of the ripple the newly-formed peak becomes almost as high as the ones at $s_{\text{w}} \approx 0.4$ m and at $s_{\text{w}} \approx 1.7$ m. Just as in the co-injection case, the maximum of the peak at $s_{\text{w}} = 2.0$ m corresponds to $R \approx 2.1$ m and furthermore, to the minimum of the E_{r} profile at $\rho \approx 0.96$ on the horizontal midplane (see figure 3). The wall power flux has a similar shape to the particle flux, and the peak power flux onto the wall is 0.25 MW m^{-2}.

The divertor load, shown in figure 12, is concentrated above the outer strike-point at the outer divertor ($s_{\text{d}} = 0.7$–0.9 m). Without the ripple the peak wall load is about 15% of the peak divertor load, whereas with the ripple the ratio of the peak load is about one over four. The ripple increases the peak wall loads, especially in the passive stabilizer loop, and decreases the divertor load. This is also apparent from tables 1 and 2. The shape of the divertor load does
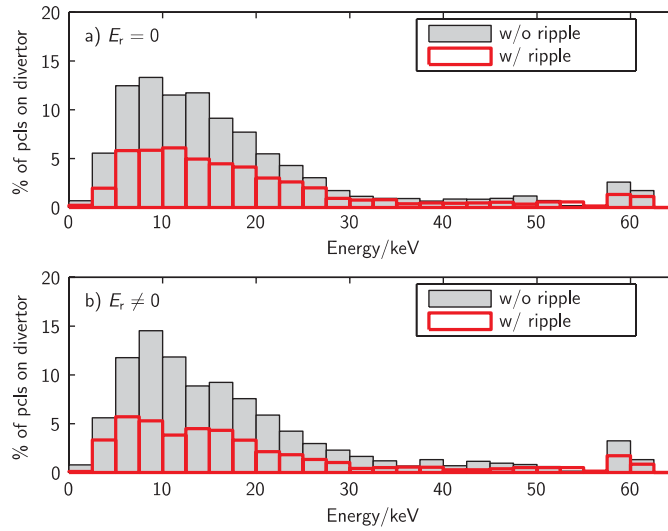
Figure 8. The energy distribution of the particle flux onto the divertor in the axisymmetric case (grey bars) and in the case with finite toroidal ripple (red/grey thick-lined bars) for co-injected neutral beams (H-mode) as percentages of the total number of lost particles. (*a*) No E_r. (*b*) Typical QH-mode E_r, shown in figure 3.
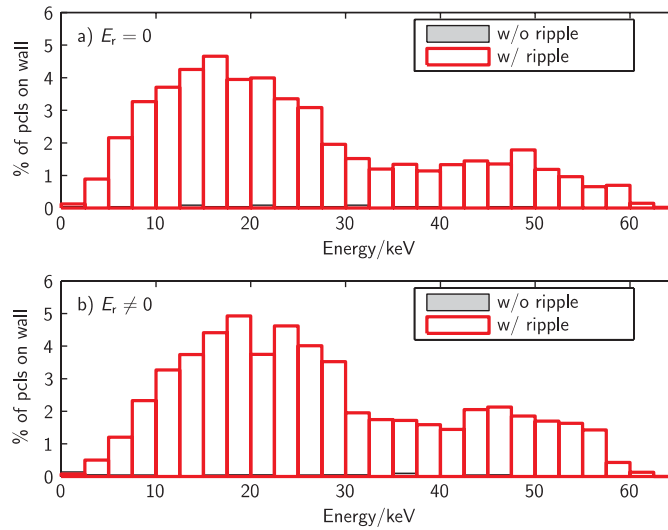

Figure 9. The energy distribution of the particle flux onto the wall structures in the axisymmetric case (grey bars) and in the case with finite toroidal ripple (red/grey thick-lined bars) for co-injected neutral beams (H-mode) as percentages of the total number of lost particles. (*a*) No E_r. (*b*) Typical QH-mode E_r, shown in figure 3.

not change with the ripple. As with the wall load, the divertor power flux and particle flux have a similar shape, and the peak power flux is $0.5\,\mathrm{MW\,m^{-2}}$.

The prompt losses of particles are apparent also from the energy distribution of the wall hits in figure 13 showing peaks near 60, 30 and 20 keV corresponding to full, half and one-third energy components of the nominal beam energy. For this reason the average energy of the
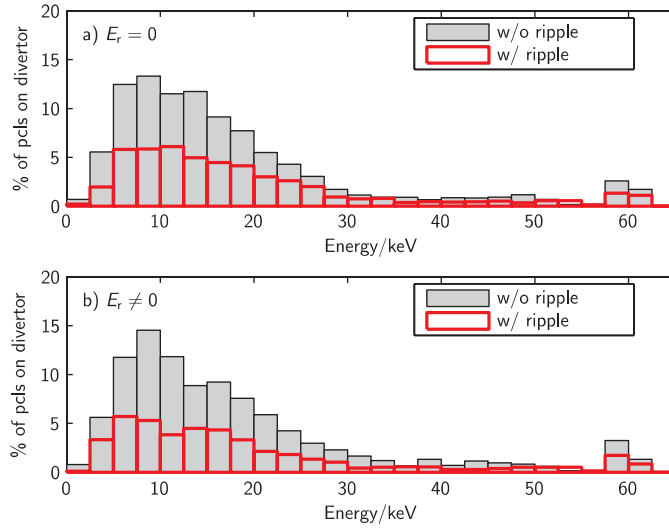
Figure 10. The toroidal distribution of the particle flux (*a*) onto the divertor and (*b*) onto the wall structures as percentages of the total number of lost particles with (red/grey thick-lined bars) and without E_r (grey bars) in the case with finite toroidal ripple for co-injected neutral beams (H-mode). The TF coils are located at $\phi = 0°$ (mod 22.5°).
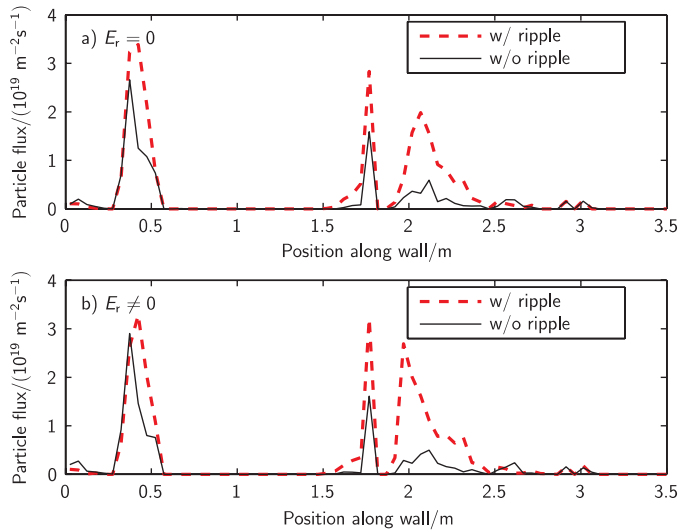

Figure 11. The particle flux onto the wall structures in the axisymmetric case (——) and in the case with finite toroidal ripple (red/grey thick - - - -) for counter-injected neutral beams (QH-mode). (*a*) No E_r. (*b*) Typical QH-mode E_r, shown in figure 3. The particle flux is zero in the region $s_w > 3.5$ m in all the shown cases. The coordinates are illustrated in figure 1.

particles hitting the wall is much higher than in the co-injection simulations, as indicated in table 3. The lower average energy with finite ripple is explained by the particles that are thermalized inside the plasma without the ripple but are lost to the walls due to banana diffusion when the ripple is on. The energy distribution of the divertor particles is shown in figure 14.
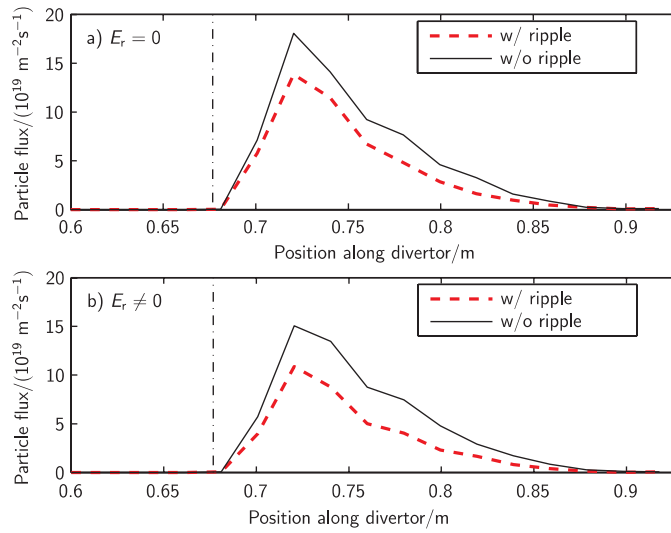
Figure 12. The particle flux onto the divertor in the axisymmetric case (——) and in the case with finite toroidal ripple (red/grey thick - - - -) for counter-injected neutral beams (QH-mode). (*a*) No E_r. (*b*) Typical QH-mode E_r, shown in figure 3. The particle flux is zero in the region $s_w < 0.6$ m in all the shown cases. The strike-points are marked with vertical dash–dot lines, and the coordinates are illustrated in figure 1.
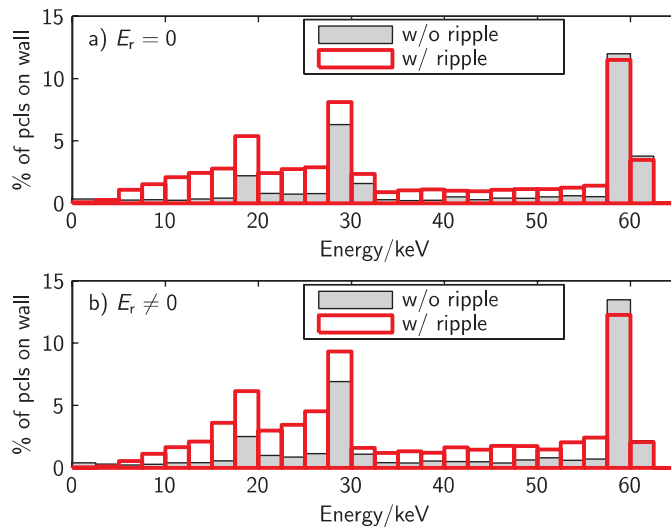

Figure 13. The energy distribution of the particle flux onto the wall in the simulation without (grey bars) and with ripple (red/grey thick-lined bars) for counter-injected neutral beams (QH-mode) as percentages of the total number of lost particles. (*a*) No E_r. (*b*) Typical QH-mode E_r, shown in figure 3.

The toroidal distributions of the wall load for the co- and counter-injection cases are clearly peaked at about halfway between the TF coils, as can be seen in the lower halves of figures 10 and 15, respectively. In the co-injection case the peak is slightly shifted towards smaller angles, but otherwise the distributions seem similar. A closer inspection, however, reveals that in the
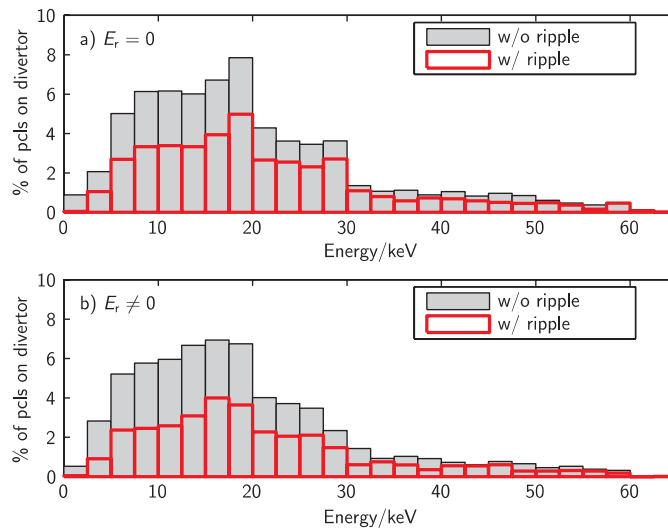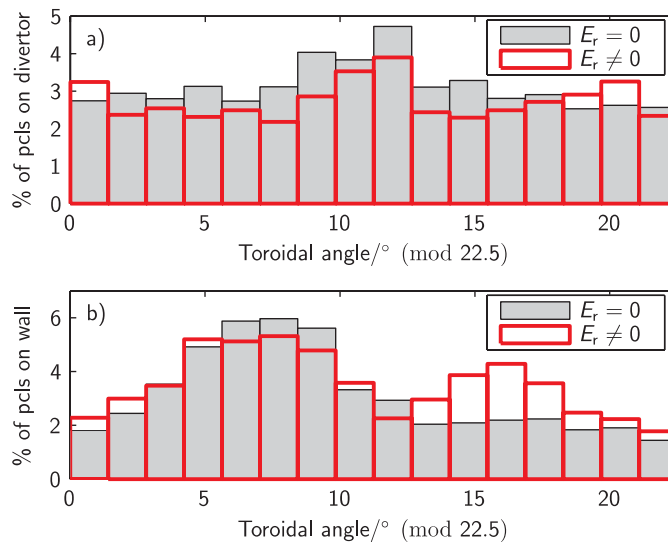
Figure 14. The energy distribution of the particle flux onto the divertor in the axisymmetric case (grey bars) and in the case with finite toroidal ripple (red/grey thick-lined bars) for counter-injected neutral beams (QH-mode) as percentages of the total number of lost particles. (*a*) No E_r. (*b*) Typical QH-mode E_r, shown in figure 3.

Figure 15. The toroidal distribution of the particle flux (*a*) onto the divertor and (*b*) onto the wall structures as percentages of the total number of lost particles with (red/grey thick-lined bars) and without E_r (grey bars) in the case with finite toroidal ripple for counter-injected neutral beams (QH-mode). The TF coils are located at $\phi = 0°$ (mod 22.5°).

counter-injection cases with and without E_r the peak consists mostly of particles with small pitch, and the full, half and one-third energy components of the nominal beam energy are missing. Together with the location of the peak this indicates that the peak originates from the particles which have had enough time to slow down from their initial energy and then have become ripple-trapped. In contrast there is nothing special either in the pitch or energy

distribution of the particles forming the peak in the co-injection case without E_r. However, with E_r, a secondary peak forms at $\phi \approx 16°$ (mod 22.5°). This peak is similar in nature to the peaks in the counter-injection cases, i.e. it consists of particles with small pitch and decreased energy, and it probably corresponds to the peak in the wall particle flux in figure 11. No secondary peak appears in the counter-injection case with E_r, but the solitary peak becomes higher while the surroundings stay at their previous level.

The fluctuations in the toroidal distribution of the divertor load with ripple, illustrated in the upper halves of figures 10 and 15, are as large as those without ripple (not shown). In axisymmetric simulations the fluctuations in the toroidal distribution are statistical. This means that any toroidal dependence caused by the ripple is too small to be detected. This is understandable because the sheared q-profile in the SOL-region causes the field lines to fan out on the target plates.

The particle fluxes onto the wall are artificially low in all the simulation cases because of the axisymmetric two-dimensional wall used in ASCOT. In reality the wall is not axisymmetric, and the fast particles hit only the limiter surfaces and predominantly the part which is closest to the plasma. Even without considering the effect of the two-dimensional wall, the simulated peak wall loads are higher than the average loads shown in figures 6 and 11 because of the uneven toroidal distribution caused by the ripple. The peak-to-average ratio of the toroidal distribution is 2.0 with co-injection and 2.3 with counter-injection (see figures 10 and 15). The peak wall loads with the toroidal distribution taken into account are then $0.1\,\mathrm{MW\,m^{-2}}$ and $0.6\,\mathrm{MW\,m^{-2}}$ with co- and counter-injection, respectively. The divertor load is more evenly distributed in the simulation, and also in reality the divertor is close to being axisymmetric. Therefore the simulated divertor loads are more realistic.

3.2. Fast ion edge distribution

From the same simulations as the wall and divertor loads we also get the different fast ion edge distributions listed in section 2.2. First we discuss the radial densities in all the eight simulations shown in figure 16. In the counter-injection cases (QH-mode), the density of fast ions in the edge pedestal region ($\rho \approx 0.95$) is always higher than in the corresponding co-injection simulations (H-mode). For this reason also the edge density gradient is steeper in the counter-injection case. The ripple always reduces the density, except at the very edge of the plasma. Therefore the ripple decreases the density gradient in both the cases. The effect of the radial electric field is too small to be seen.

The total velocity distributions in figure 17 give a more detailed comparison between the co- and counter-injection cases without the ripple and E_r. Also from this figure the larger population of counter-injected ions in the QH-mode edge and the resulting steeper density gradient are apparent, especially at higher velocities. Although not shown, the situation is the same also in the other simulation cases with different combinations of the ripple and E_r.

Figure 18 shows the comparison of the perpendicular velocity distribution in the co- and counter-injection cases without the ripple and E_r. With counter-injection, most of the particles in the steep gradient region ($\rho > 0.95$) have $v_\perp \approx 10^6\,\mathrm{m\,s^{-1}}$, whereas with co-injection the maximum of the $v_\perp$-distribution is closer to zero. This difference can be explained as follows: near the separatrix the plasma density is low and hence, the neutral beam particles have small ionization probability. The co-injected particles are born on well-confined orbits opening inwards, and for this reason there are only a few particles on banana orbits in the steep gradient region in the co-injection case. The counter-injected particles ionized near the separatrix are lost promptly to the walls, but the particles ionized further inside the plasma are born on
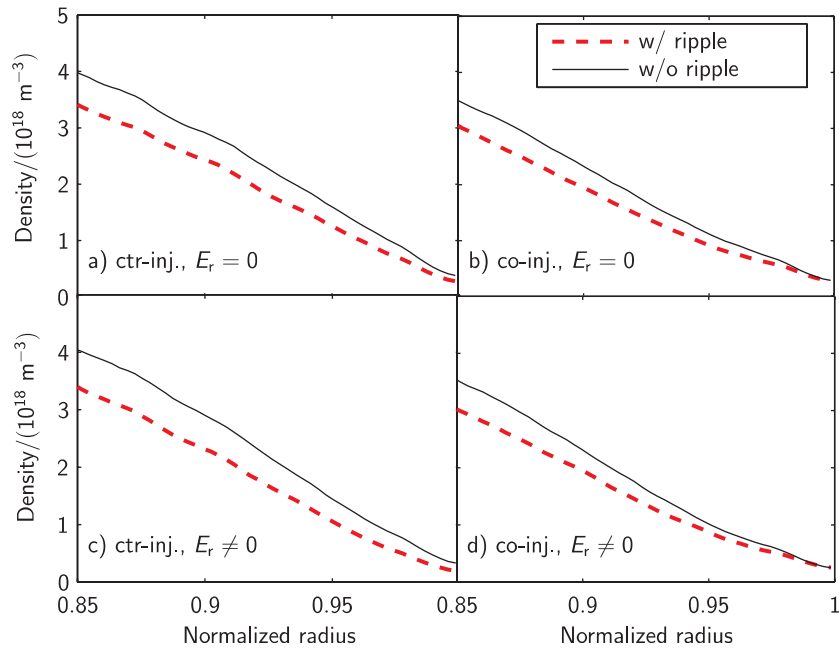
Figure 16. The radial density of fast ions with (red/grey thick – – –) and without ripple (——) in different cases: (*a*) counter-injection, no E_r, (*b*) co-injection, no E_r, (*c*) counter-injection, typical QH-mode E_r and (*d*) co-injection, typical QH-mode E_r.
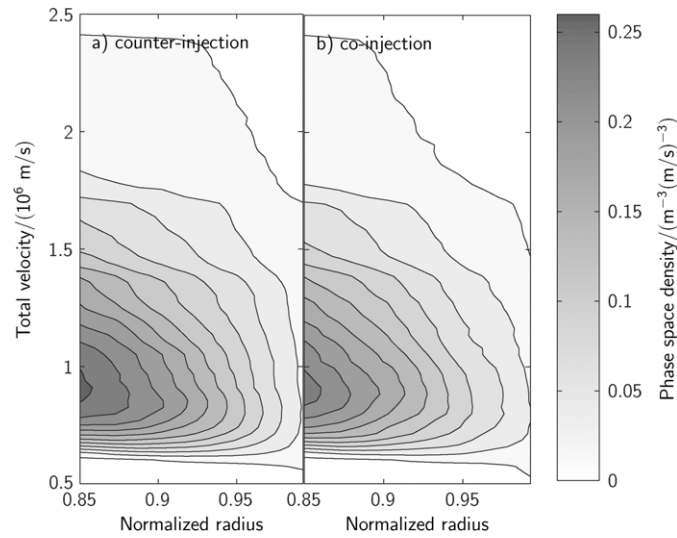

Figure 17. The total velocity distribution of fast ions without ripple and E_r for (*a*) counter-injection and (*b*) co-injection. The contour levels in (*a*) and (*b*) are the same for easier comparison.

banana orbits opening outwards, which constitute the majority of the $v_\perp$-distribution in the steep gradient region.

Next we discuss the effects of E_r, which show best in the parallel velocity distribution. In figures 19 and 20 the parallel velocity distributions with and without E_r are compared in the
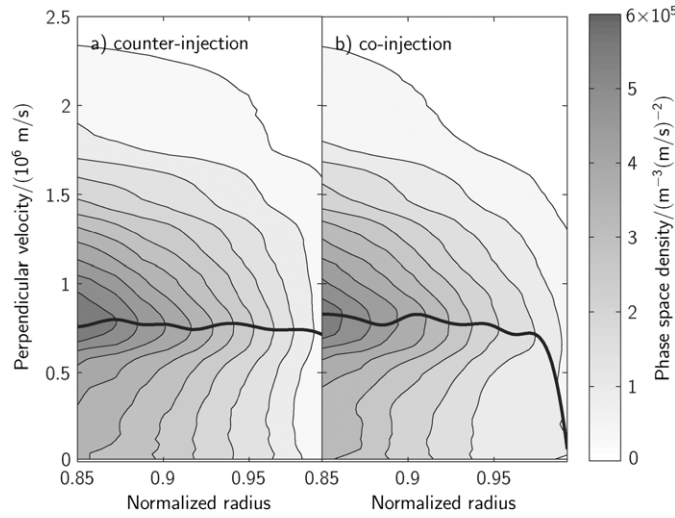
Figure 18. The perpendicular velocity distribution of fast ions without ripple and E_r for (*a*) counter-injection and (*b*) co-injection. The thick lines (——) show the maximum points of the distributions in the $v_\perp$-direction. The contour levels in (*a*) and (*b*) are the same for easier comparison.
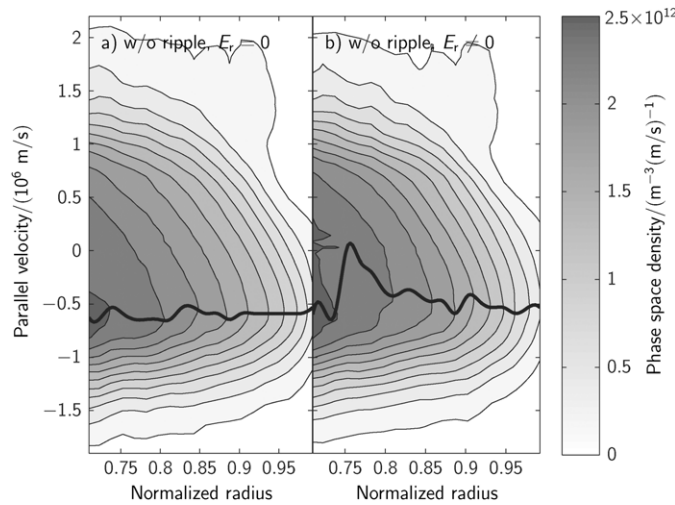

Figure 19. The parallel velocity distribution of fast ions in the axisymmetric counter-injection simulation (*a*) without E_r and (*b*) with E_r. The thick lines (——) show the maximum points of the distributions in the $v_\parallel$-direction. The contour levels in (*a*) and (*b*) are the same for easier comparison.

axisymmetric case and in the case with the non-vanishing ripple, respectively. The bump in the upper part of each distribution is produced by particles born on passing orbits, since there is no mirror image on the $v_\parallel < 0$ side, and by particles born on banana orbits but lost to the wall before reflecting. Any particles with negative $v_\parallel$ has been slowing down for at least the duration of one orbit.

The maximum point on the distribution in the $v_\parallel$-direction is always negative. This is caused by the monotonic q-profile: a particle on the outer half of its banana orbit has to move
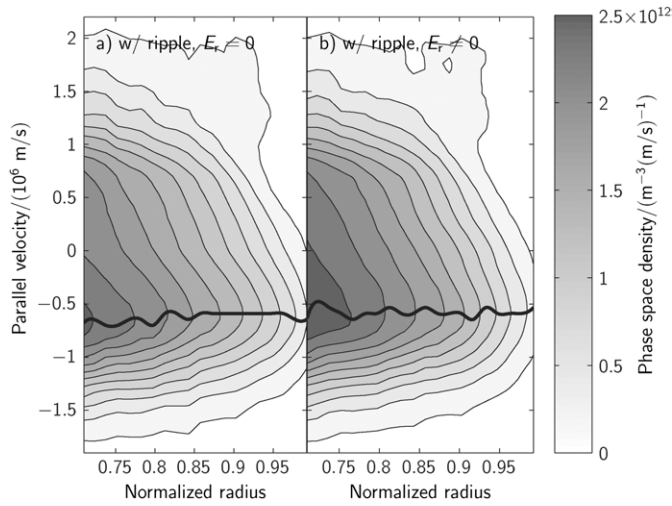
Figure 20. The parallel velocity distribution of fast ions (*a*) without E_r and (*b*) with E_r in the counter-injection simulations with finite ripple. The thick lines (——) show the maximum points of the distributions in the $v_\parallel$-direction. The contour levels in (*a*) and (*b*) are the same for easier comparison.

farther in the toroidal direction than a particle on the inner half in order to complete the half-orbit. On the outer half-orbit the $v_\parallel$ of a particle is negative, and so the particles end up spending more time on negative values of $v_\parallel$. The same holds also for the co-injected particles. On the other hand, because the particles spend most of the time at the banana tips and because the distribution is averaged over poloidal angle, the maximum is always relatively close to zero.

Judging from the figures, the effect of E_r is to remove particles with negative $v_\parallel$ or to transform them to positive $v_\parallel$. Without E_r the distribution is skewed with respect to $v_\parallel$, but with E_r the distribution is more symmetric. The effect is most visible in figure 19, but it is also present in figure 20. The ripple, on the other hand, removes particles with small $v_\parallel$, thereby causing the level curves to become concave near $v_\parallel \approx 0$. This is consistent with the observation that the peak in the toroidal wall distribution of counter-injected particles, cf figure 15, contains mostly particles with the low pitch.

In the H-mode the differences between the cases with and without E_r are much smaller, but the observations appear consistent with the QH-mode findings.

4. Tritium surface distribution

The long-term tritium retention will be a critical issue in future fusion reactors. Tritium can be co-deposited with the eroded first wall material, but in D–D discharge machines the tritium distribution on the plasma-facing components has been found to be similar to the distribution of high-energy triton implantation [18, 19]. To confirm these findings, the surface distribution of tritons born from beam–plasma and plasma–plasma D–D reactions was simulated. Since the amount of implanted tritium per unit area on the material surfaces corresponds to the time-integrated particle flux, neglecting the decay, it suffices to study the incoming triton flux.

The measured tritium in the surface materials has been accumulating over time and during various kinds of discharges, of which the H-mode is the most typical one. To successfully simulate this distribution, a background from the H-mode discharge #17219 at $t = 2.5\,\text{s}$
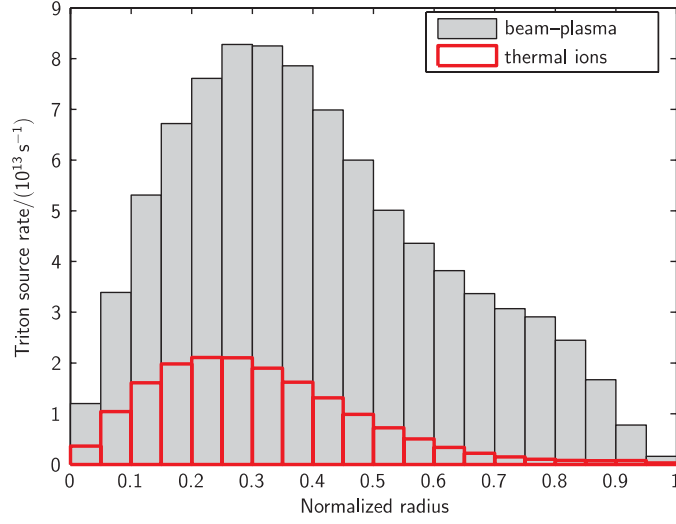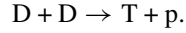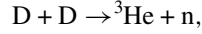
Figure 21. The triton source rate for beam–plasma (grey bars) and plasma–plasma (red/grey thick-lined bars) reactions used in the simulations.

was used instead of the QH-mode background used in the previous sections. The tritons are produced in one of the two D–D reaction branches,

$$D + D \rightarrow {}^3He + n,$$
$$D + D \rightarrow T + p.$$

Equal reaction rates are assumed for the two branches, so that the measured neutron rate is equal to the triton source rate. The initial energy of tritons is 1.008 MeV, and in the simulations the pitch was assumed to be uniformly distributed. This is a reasonable assumption, since the initial energy of tritons is high even compared with the nominal injection energy of the neutral beams. Figure 21 shows the calculated source rate of tritons as a function of ρ. Due to the fast parallel motion of beam ions, the tritons were assumed to be born uniformly along a flux surface.

An ensemble of 12 500 test particles was used and the particles were given weights according to the local volume element along a single flux surface and according to the triton source rate in the ρ-direction. The particles were simulated with and without ripple until they were thermalized, and the hits on the material surfaces were recorded.

In the axisymmetric case, 13% of the tritons hit the divertor and 16% the wall. With the ripple the fraction of particles hitting the divertor decreases slightly to 11%, but the wall load is increased up to 24% of the total number of particles. Figure 22 shows the triton flux onto the divertor and onto the wall. The divertor flux is practically the same with and without the ripple, but on the wall the flux onto the guard limiter ($s_w \approx 1.5$ m) is significantly higher with the ripple.

Figure 23 shows the toroidal distribution of the triton flux on the divertor and on the wall. As in the simulations of the co-injected neutral beams, with the ripple there is a peak in the wall load, but interestingly it is in a different place, to the left of each TF coil. The divertor load is always uniform in the toroidal direction.

The simulation results were compared with photo-stimulate luminescence (PSL) measured from the divertor and wall tiles, shown in figures 24 and 25, respectively. The simulation results are in qualitative agreement with the experimental results. The divertor results are especially
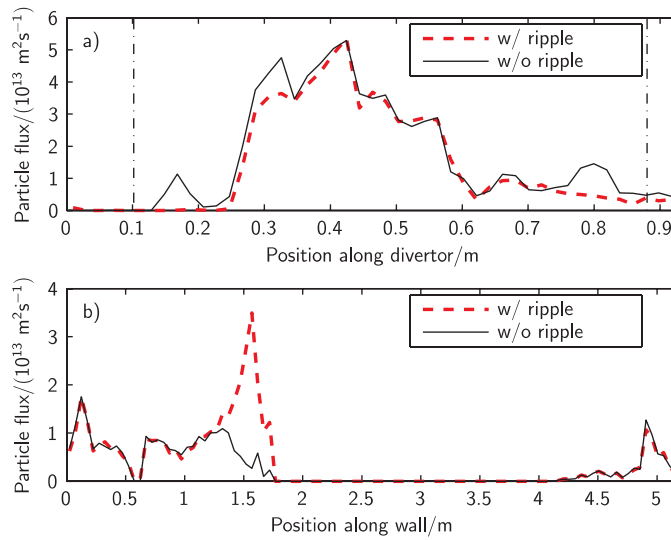
Figure 22. The triton flux (*a*) onto the divertor and (*b*) onto the wall structures in the axisymmetrical case (——) and in the case with finite toroidal ripple (red/grey thick - - - -). The strike-points are marked with vertical dash–dot lines in (*a*) and the coordinates are illustrated in figure 1.
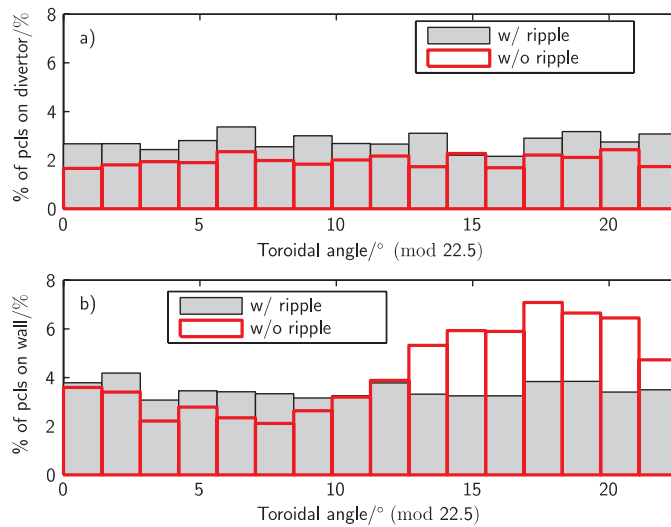

Figure 23. The toroidal distribution of the triton flux (*a*) onto the divertor and (*b*) onto the wall structures in the axisymmetrical case (grey bars) and in the case with finite toroidal ripple (red/grey thick-lined bars).

good, although in the simulation there is almost no flux at the strike-points. This is probably due to the fact that the simulated flux consist almost exclusively of high-energy tritons, whereas in the experimental results the thermal load is also included. The ELMs, for instance, cause a flux of particles onto the strike-points which, at present, cannot be reproduced in ASCOT simulations.

On the wall the shape of the simulated flux is roughly the same as the shape of the measured PSL intensity, but the PSL intensity on the wall, and especially in the vicinity of the guard
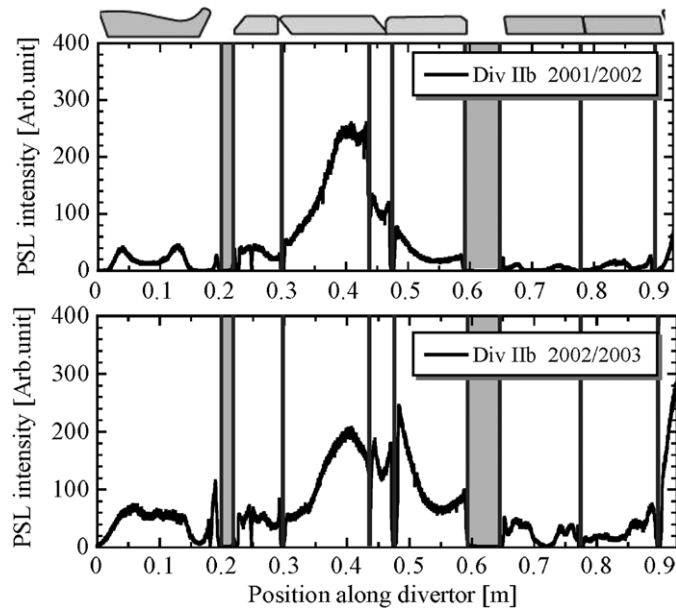
Figure 24. The measured PSL intensity on the divertor from ASDEX Upgrade campaigns 2001/2002 and 2002/2003.
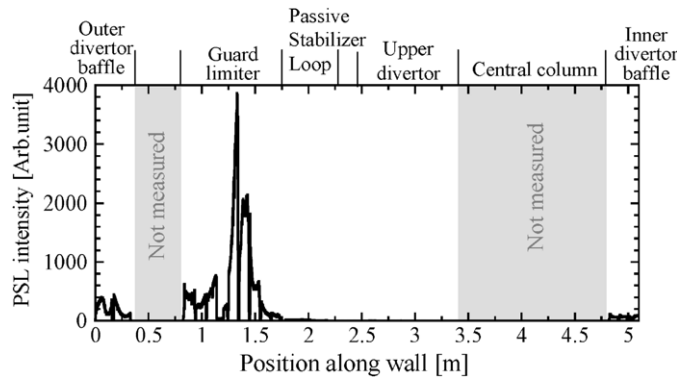

Figure 25. The measured PSL intensity on the wall from ASDEX Upgrade campaign 2002/2003.

limiter, is an order of magnitude higher than on the divertor. In the simulation results this is not the case but, as in the case of the fast ion wall load, this can be attributed to the two-dimensional wall which falsely decreases the wall load. The missing thermal tritons might also play a role, since the larger particle flux to the wall in the simulation with the ripple is mostly due to the thermal particles which end up at the guard limiter. The average energy of the particles hitting the guard limiter is roughly 850 keV, but with the ripple it is smaller, about 600 keV. This allows one to speculate that thermal or near-thermal tritons emerging from the plasma would hit the guard limiter and increase the flux.

The tritium simulation results are still somewhat preliminary: only one discharge has been simulated, whereas the measured tritium has been accumulating over the whole experimental campaign. Therefore it may be necessary to simulate a large number of different discharges to get the time-integrated tritium inventory in the surfaces.

5. Conclusions

The ASDEX Upgrade H-mode and QH-mode have been compared by ASCOT-simulations of co- and counter-injected neutral beam ions, respectively. The quantities of interest were the particle flux onto the wall and the divertor and the fast ion edge distribution. Additionally, the flux of high-energy tritons resulting from beam–plasma and thermal D–D interactions has been evaluated and compared with the measured tritium distribution in the divertor and wall tiles.

In the QH-mode, corresponding to the counter-injected neutral beams, the wall load is substantial even without the toroidal ripple, whereas in the H-mode, corresponding to the co-injected neutral beams, the ripple is required to create any significant wall load. In all the cases the wall load is increased by the ripple, but the divertor load is either decreased (QH-mode) or unchanged (H-mode). Additionally, the ripple causes a peak in the toroidal distribution of the wall load approximately halfway between the toroidal field coils in both the H-mode and the QH-mode.

The effect of the radial electric field E_r alone is small, but together with the ripple it creates a peak in the wall load at $R \approx 2.1$ m, which on the horizontal midplane corresponds to the minimum of the E_r profile. The particles forming the peak become trapped near the horizontal midplane due to the combined effect of the E_r and ripple and, subsequently, drift up or down in the direction of the ∇B-drift. Therefore the location of the peak along the wall is different for the H-mode and QH-mode cases. In the H-mode these particles form a secondary peak in the toroidal distribution, which does not happen in the QH-mode. A positive radial electric field in the SOL is likely to affect the wall load, but the measurements of such a field were not available for the simulations.

With co-injection, the peak divertor and wall power loads are $0.2\,\mathrm{MW\,m^{-2}}$ and $0.1\,\mathrm{MW\,m^{-2}}$, respectively. With counter-injection the numbers are $0.5\,\mathrm{MW\,m^{-2}}$ and $0.6\,\mathrm{MW\,m^{-2}}$. The wall load can be considered as a lower limit, because in the simulations its numerical value is artificially brought down by the two-dimensional wall. The simulated loads can be compared with the experimental H-mode steady-state loads, which are between 1 and $2\,\mathrm{MW\,m^{-2}}$ on the divertor, depending on the NBI input power, and up to $1\,\mathrm{MW\,m^{-2}}$ on the leading edge of the limiters.

The fast ion density and its gradient in the pedestal region are higher in the QH-mode than in the H-mode. Also the perpendicular velocity, and hence the pitch distribution, is different for the co- and the counter-injected particles. The significance of these differences for the edge stability could be evaluated by using the simulated particle distributions as the input for MHD stability codes.

The ripple, with or without E_r, removes particles with low $v_\parallel$ by ripple-trapping, and this is reflected in the toroidal distribution of the wall losses, in which the majority of the particles forming the peak have low pitch value. It also shows in the parallel velocity distribution as the concavity of the level curves near $v_\parallel \approx 0$.

The simulated triton flux is in qualitative agreement with the measured tritium distribution, but a more detailed study comprising a large number of different discharges may be necessary, since the single simulated discharge is unlikely to represent the whole experimental campaign accurately.

carried out within the framework of the European Fusion Development Agreement. The views and opinions expressed herein do not necessarily reflect those of the European Commission. The computations presented in this document have been made with the CSC's computing environment. The CSC is the Finnish IT center for science and is owned by the Ministry of Education.

References

[1] Zohm H 1996 *Plasma Phys. Control. Fusion* **38** 105–28
[2] Nave M F F *et al* 2000 *Plasma Phys. Control. Fusion* **42** A89–96
[3] Osborne T H *et al* 1994 *Plasma Phys. Control. Fusion* **36** A237–42
[4] Suttrop W *et al* 2005 *Nucl. Fusion* **45** 721–30
[5] Burrell K H *et al* 2002 *Plasma Phys. Control. Fusion* **44** A253–63
[6] Suttrop W *et al* 2003 *Plasma Phys. Control. Fusion* **45** 1399–416
[7] Sakamoto Y, Shirai H, Fujita T, Ide S, Takizuka T, Oyama N and Kamada Y 2004 *Plasma Phys. Control. Fusion* **46** A299–304
[8] Taylor G, Strachan J D, Budny R V and Ernst D R 1996 *Phys. Rev. Lett.* **76** 2722–5
[9] Thomas P R *et al* 1998 *Phys. Rev. Lett.* **80** 5548–51
[10] Kurki-Suonio T, Hynönen V, Suttrop W, Dux R and the ASDEX Upgrade Team 2005 *Proc. 32nd European Physical Society Conf. on Plasma Physics and Controlled Fusion combined with the 8th Int. Workshop on Fast Ignition of Fusion Targets* ed C Hidalgo and B Ph van Milligen (Madrid: European Physical Society) p P4.055 http://eps2005.ciemat.es/papers/pdf/p4_055.pdf
[11] Kurki-Suonio T, Lashkul S I and Heikkinen J A 2002 *Plasma Phys. Control. Fusion* **44** 301–23
[12] Heikkinen J A and Sipilä S K 1995 *Phys. Plasmas* **2** 3724–33
[13] Hinton F L and Hazeltine R D 1976 *Rev. Mod. Phys.* **48** 239–308
[14] Lister G G 1985 *Technical Report* 4/222, IPP Garching, Germany
[15] Conway G D, Schirmer J, Klenge S, Suttrop W, Holzhauser E and the ASDEX Upgrade Team 2004 *Plasma Phys. Control. Fusion* **46** 951–70
[16] Herrmann A 2002 *Plasma Phys. Control. Fusion* **44** 883–903
[17] Herrmann A, Eich T, Rohde V, Fuchs C J, Neuhauser J and Team A U 2004 *Plasma Phys. Control. Fusion* **46** 971–9
[18] Masaki K *et al* 2003 *J. Nucl. Mater.* **313–316** 514–8
[19] Sugiyama K, Tanabe T, Krieger K, Neu R and Bekris N 2005 *J. Nucl. Mater.* **337–339** 634–8